Folding of fiber composites with a hyperelastic matrix

Francisco López Jiménez, Sergio Pellegrino *

Graduate Aerospace Laboratories, California Institute of Technology, 1200 E. California Blvd., Pasadena, CA 91125, United States

ARTICLE INFO

ABSTRACT

This paper presents an experimental and numerical study of the folding behavior of thin composite materials consisting of carbon fibers embedded in a silicone matrix. The soft matrix allows the fibers to microbuckle without breaking and this acts as a stress relief mechanism during folding, which allows the material to reach very high curvatures. The experiments show a highly non-linear moment vs. curvature relationship, as well as strain softening under cyclic loading. A finite element model has been created to study the micromechanics of the problem. The fibers are modeled as linear-elastic solid elements distributed in a hyperelastic matrix according to a random arrangement based on experimental observations. The simulations obtained from this model capture the detailed micromechanics of the problem and the experimentally observed non-linear response. The proposed model is in good quantitative agreement with the experimental results for the case of lower fiber volume fractions but in the case of higher volume fractions the predicted response is overly stiff.

© 2011 Elsevier Ltd. All rights reserved.

1. Introduction

Deployable space structures have traditionally been based around stiff structural members connected by mechanical joints, but more recently joint-less architectures have been proposed. In this case large relative motions between different parts of a structure are achieved by allowing the connecting elements to deform elastically. For example, deployable solar arrays consisting of sandwich panels connected by tape spring hinges make use of cylindrical thin shells to provide the connection between the panels. This connection becomes highly compliant when elastic folds are created in the tape springs, allowing the panels to stow compactly, but it becomes much stiffer when the tape springs are allowed to deploy and snap back into the original configuration. The maximum curvature of the tape springs cannot exceed a limiting value that is related to the failure strain of the material (Rimrott, 1966; Yee et al., 2004).

Tape spring hinges have been made from metal (Watt and Pellegrino, 2002; Auternaud et al., 1993), carbon fiber composites (Yee et al., 2004; Yee and Pellegrino, 2005), and memory matrix composites (Campbell et al., 2005; Barrett et al., 2006). This last approach makes use of polymers that become softer above a transition temperature and these materials have been exploited to make hinges that can be heated and folded to very high curvatures. When they are cooled the hinges remain "frozen" in the folded configuration but will then self-deploy when they are re-heated. A variant of

this approach is to use a very soft elastic matrix, orders of magnitudes softer than standard epoxies; in this way the same type of behavior can be achieved without the need to heat the material. The reason is that the fibers on the compression side of the material can form elastic microbuckles and so, instead of being subject to a large compressive strain, they are mainly under bending.

This approach has already been exploited by Datashvili et al. (2005) who used a silicone matrix and by Mejia-Ariza et al. (2006) and Rehnmark et al. (2007) who used other approaches. Models showing exceptional folding capabilities have been demonstrated (Datashvili et al., 2010; Mejia-Ariza et al., 2010).

A number of simplified analytical models of this behavior have been already developed, see Section 2 of this paper, however these models do not capture the detailed micromechanics of the fibers and matrix and so their predictive capability is limited. Our long-term objective is to establish experimentally validated models for the folding behavior of a thin composite consisting of unidirectional carbon fibers embedded in a silicone matrix. Such models would be used to predict the strain in the fibers for any given, overall curvature and hence to estimate the failure curvature of any specimen with known properties and to study a variety of related effects, such as estimating the bending stiffness of a composite of stiff fibers embedded in a soft matrix, allowing for the softening associated with microbuckling.

A key question that arises when developing such models is what assumptions are justified to reach an effective compromise between model complexity and ability to obtain physically representative predictions. In the present study we focus on two key effects, fiber distribution and large strain hyperelastic behavior of the matrix without any damage or other dissipation sources.

* Corresponding author.
   E-mail address: sergiop@caltech.edu (S. Pellegrino).

Damage effects have been considered in a separate paper (López Jiménez and Pellegrino, 2011).

The paper is laid out as follows. Section 2 presents a review of some relevant literature. Section 3 details the material properties and fabrication process, as well as an analysis of fiber distribution based on micrographs of actual specimens. Section 4 presents the experimental results of a folding test that shows evidence of microbuckling in the material; a characterization of the non-linear moment–curvature relationship of the material is also obtained. It is shown that, in addition to fiber microbuckling, there is evidence of damage-related stress-softening. Section 5 describes the finite element model used to study in detail the behavior of a periodic unit cell based on a representative volume element (RVE) including a small number of elastic fibers, typically between ten and thirty, embedded in a hyperelastic matrix. The RVE has a length longer than the buckle wavelength. Section 5.2 discusses two different fiber arrangements used in the simulations. The first one is a hexagonal pattern, characterized only by the fiber volume fraction in the material. The second starts from a random distribution of fibers that is rearranged until it matches the distribution observed in actual micrographs. The predictions for buckle wavelength and moment–curvature relationship obtained from the finite element model are compared with the experimental results in Section 6. Section 7 summarizes the findings of this work and concludes the paper.

2. Background

The literature relevant to the present study can be categorized under three main headings: elastic fiber microbuckling, large straining of soft materials with embedded fibers, and strain softening.

Regarding the first topic, fiber microbuckling is a well known failure mode for composite materials, see the review in Fleck (1997). Rosen (1965) proposed a model based on the buckling of a beam on an elastic foundation; he assumed a sinusoidal shape for the buckled fibers and compared the work done by the external forces with the strain energy in the system. He considered two different buckling modes. In the first one the matrix deforms in extension, while in the second one it shears. The second mode requires a lower critical load and it is therefore considered the preferred one. Rosen's approach of treating the fibers as beams on an elastic foundation has been used by several other authors to explore the effects of material thickness, fiber volume fraction and type of load, see for example Drapier et al. (1996, 1999, 2001) and Parnes and Chiskis (2002).

Microbuckling has been invoked as a stress relieving mechanism in thermoplastic and elastic memory composites that are subject to large bending curvatures (Campbell et al., 2004; Marissen and Brouwer, 1999; Murphey et al., 2001). Fig. 1 shows a sketch that explains this behavior. When folding starts, the

extensional stiffness is uniform through the thickness and hence the neutral axis lies in the middle plane. As the fibers on the compression side reach the critical buckling load, their stiffness is reduced in the post-buckling range and this corresponds to a bilinear constitutive model that shifts the neutral axis towards the tensile side of the laminate. This effect reduces both the maximum tensile and the maximum compressive strain in the fibers, allowing them to remain elastic for much higher curvatures than if the fibers had remained unbuckled. It should be noted that in Fig. 1 the buckling deflection has been depicted as out of plane for a better visualization, but experimental observations show that in most cases it occurs within the plane of the material, that is, parallel to the axis of bending.

This effect has been studied by Francis et al. (2006) and Francis (2008) who provided the following approximation for the fiber buckle wavelength:

$$\lambda = \frac{\pi}{2}\left(\frac{9 V_f t^2 d^2 E_f}{8 G_m \ln\left(\frac{6t}{d}\sqrt{\frac{V_f}{\pi}}\right)}\right)^{\frac{1}{4}} \tag{1}$$

where d is the fiber diameter, t is the thickness of composite plate being bent, E_f is the stiffness of the fibers, G_m is the shear modulus of the matrix, and V_f is the fiber volume fraction.

The amplitude of the buckle waves can be obtained from

$$a = \frac{2\lambda}{\pi}\sqrt{\kappa(z - z_n)} \tag{2}$$

which relates the geometry of the buckled state with the applied curvature κ and the distance to the neutral axis $z - z_n$. The maximum strain in the fibers can then be obtained with:

$$|\epsilon_f| = \frac{d}{2}\kappa_f = \frac{d}{2}v'' = \frac{da\pi^2}{2\lambda^2} \tag{3}$$

Studies of elastic memory composites (Campbell et al., 2005; Schultz et al., 2007) and also of carbon–fiber composites with a silicone matrix (López Jiménez and Pellegrino, 2009) have extended Rosen's model and all assumed small strains and a linear constitutive relationship both for the fibers and the matrix.

Turning to the second topic, large strain formulations for fiber reinforced composites were investigated by Merodio and Ogden (2002, 2003). Their model, based on Spencer (1972), introduces two invariants to model the effect of the incompressible fibers on the strain energy of the material. Following Geymonat et al. (1993), the appearance of macroscopic instabilities is related to the loss of ellipticity of the homogenized constitutive relationships. Several biological materials, such as the cornea or blood vessels, fit the description of stiff fibers in a very soft matrix and models based on such an approach have been used by Holzapfel et al. (2000), Pandolfi and Manganiello (2006), Pandolfi and Holzapfel (2008). The second order homogenization theory developed by Ponte Castañeda (2002) has also been applied to fiber-reinforced hyperelastic materials. This approach is still under development, see for example Lopez-Pamies and Ponte Castañeda (2006), Agoras et al. (2009) and Lopez-Pamies and Idiart (2010); a comparison to numerical results has been presented in Moraleda et al. (2009b). In all of these studies the loading is two dimensional, usually under the assumption of plane strain. To the authors' knowledge, there is no detailed experimental or theoretical analysis of fiber reinforced soft materials under bending, which is the situation most relevant to the present study.

The final topic is strain softening, of a type known to occur in particle reinforced rubbers, such as tires. Their behavior is shown schematically in Fig. 2. If a virgin material sample is loaded to the strain level (1) it follows the path (a), known as the primary
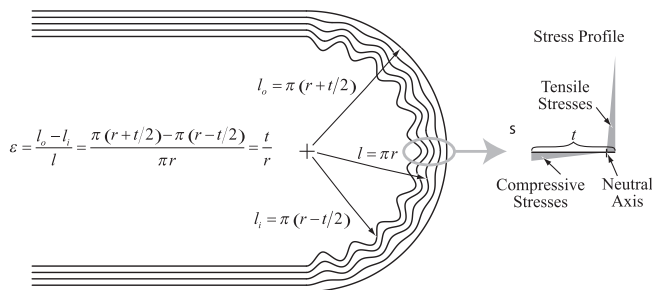

Fig. 1. Fiber microbuckling and stress profile in a heavily bent laminate, taken from Murphey et al. (2001).
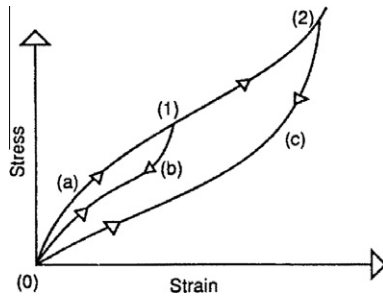
Fig. 2. Schematic of cyclic tension demonstrating Mullin's effect. Taken from Govindjee and Simo (1991).

loading curve. Subsequent unloading and loading to (1) will follow the path (b) as the material has been weakened by the initial loading process and so its stiffness is reduced. If the strain exceeds (1) path (a) is joined again. If unloading from a higher strain level (2) occurs, it will create a new path (c) with an even greater loss of stiffness. This type of behavior is usually called Mullins' effect.

The process described above is somewhat idealized as in reality there is a stress reduction on each successive loading and unloading cycle. The reduction is largest between the first and second cycle, and it becomes very small after a few cycles, a process known as preconditioning. After these initial cycles the stress–strain response is essentially repeatable. Representing the loading and unloading path as coincident is also an idealization. There are large differences in the stress in both states, even in rubbers not showing hysteresis before being reinforced. All these phenomena depend on the concentration of particles in the rubber. In particular, both the softening and the hysteresis increase with the filler content. Several models for stress-softening have been proposed, see for example Govindjee and Simo (1991) or Dorfmann and Ogden (2004).

Stress softening is also common in biological tissues, including tissues composed of collagen fibers in soft matrix (Fung, 1972; Holzapfel et al., 2000). In general, stress softening can be eliminated by preconditioning the material.

3. Specimen fabrication and characterization

3.1. Fabrication

The fibers were HTS40-12K, produced by Toho Tenax (retrieved August 2010) and provided by the Itochu Corporation in the form of a uniaxial ply of dry fibers with an areal density equal to 40 g/m^2. This implies that every 12 K tow has been spread to a width of approximately 20 mm, although the separate tows are almost indistinguishable. The properties of the fibers are provided in Table 1; note that only longitudinal properties were obtained. Comparative studies using typical values for the remaining properties were performed in Section 5.1.

Table 1
Material properties provided by the manufacturers.

Fiber properties	
Diameter	7 μm
Longitudinal modulus	240 GPa
Density	1.77 g/cm^3
Strain at failure	1.8%
Matrix properties	
Viscosity (part A)	1300 mPa s
Viscosity (part B)	800 mPa s
Density	0.96 g/cm^3
Tensile modulus	0.8 MPa
Strain at failure	100%

The matrix material was CF19-2615, produced by NuSil Silicone Technology (March 2007). This is a two part, optically clear silicone chosen for its low viscosity (see Table 1) in order to facilitate its flow within the fibers.

The fabrication process was as follows. First the two parts of the silicone were mixed, then vacuum was applied to extract air bubbles and finally the mixture was poured over the fibers, previously placed on either a Teflon coated tray for the case of specimens cured in an oven or on a PTFE sheet for specimens cured in an autoclave. Both types of specimens were cured for 30 min at 150 °C. In the case of autoclave curing the specimens were vacuum bagged, so internal vacuum and up to 85 psi (0.586 MPa) of external pressure were applied.

Defining the fiber volume fraction as

$$V_f = \frac{A_f}{A} \qquad (4)$$

where A_f is the cross sectional area of the fibers and A is the total area of the cross section, both observed in a micrograph, autoclave curing is able to better control V_f and hence to achieve values between 25% and 55%, see Fig. 3. Holding the specimen under vacuum is the main contributor to achieving specimens with a homogeneous fiber distribution. Increasing the pressure differential has the advantage of better consolidating the fibers and also achieving a more homogeneous distribution of fibers in the matrix.

The fiber volume fraction is fairly independent of the amount of silicone poured over the fibers. In composites cured in the autoclave, the differential pressure is enough to evacuate the extra silicone through a perforated release film. In specimens cured in the oven it is possible to obtain overall values of V_f even lower than 25% by applying an excess of silicone, but this does not result in a homogeneous distribution of the fibers. An extreme case ($V_f \approx 10\%$) can be seen in Fig. 4 where it should be noted that most of the fibers have concentrated in a narrow region and are surrounded by pure silicone. The local fiber volume fraction in the region containing the fibers is approximately 25%.

3.2. Characterization of fiber geometry

One of the goals of the numerical models presented in this paper is to study the influence of simulating a realistic fiber arrangement, as opposed to regularly arranged fibers. In order to produce such a model it is necessary to obtain micrographs of the material cross section. In composites with a harder matrix the micrographs
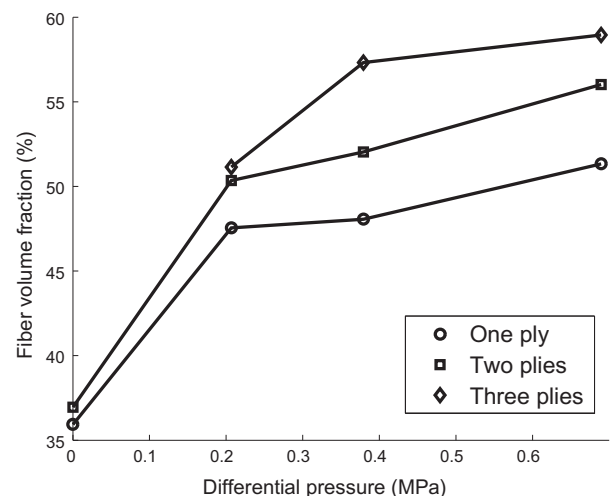

Fig. 3. Average fiber fraction vs. differential pressure applied during curing.
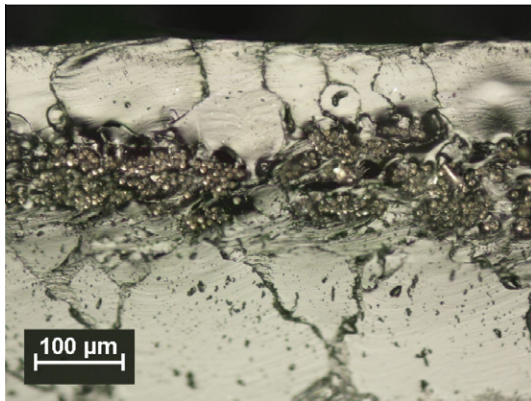
Fig. 4. Specimen with V_f = 10% overall, showing a high degree of fiber localization in the middle.

would be obtained from specimens with a flat and smooth surface, but this is not possible in the case of a very soft matrix. Instead, the material was cut with a razor blade and then placed under a Nikon Eclipse LV100 microscope with $50\times$ amplification and a Nikon DS-Fi1 digital camera. The surface obtained this way is not sufficiently flat to lie entirely within the depth of field of the microscope. In order to obtain a sharp image several pictures of the specimen were taken at different focus distances and the pictures were then processed with the focus stacking capabilities of (Adobe Photoshop CS4, 2008), see Fig. 5.

The micrographs can be used to verify measurements obtained with less precise techniques. The fiber volume fraction and thickness observed were the same as those calculated by measuring the dry weight of the fibers and the weight of the cured specimen. The micrographs show that there are 0.63 fibers per micrometre of width, which agrees with the value calculated from the weights.

The position of the fibers within the micrographs was recorded in order to obtain a statistical characterization of their arrangement. In general, the fiber arrangement can be described by the radial distribution function (RDF) which is commonly used to characterize statistically isotropic particle systems. The RDF measures the probability of finding a fiber at a given distance from the center of another fiber. Rintoul and Torquato (1997) have shown that the RDF is suitable to reconstruct systems with low particle densities, or systems with high densities in which the particles have no tendency to aggregate. The micrographs show that this is the case for the present material.

The RDF is properly defined for systems that are isotropic in all dimensions, and normalized so that it tends to one as r tends to infinity. In the present case the composite material is better idealized as a strip that is only isotropic in one dimension. Instead of using the RDF, the second-order intensity function $K(r)$ (Pyrz, 1994a,b) was used. $K(r)$ is defined as the number of fibers expected to lie within a radial distance r from an arbitrary fiber, normalized
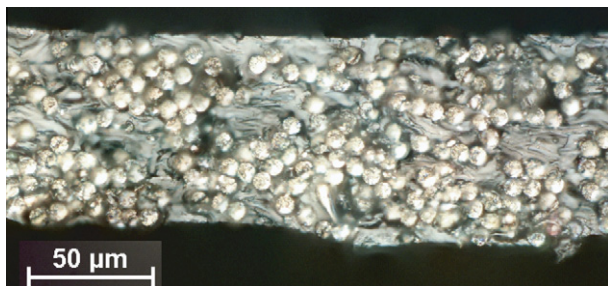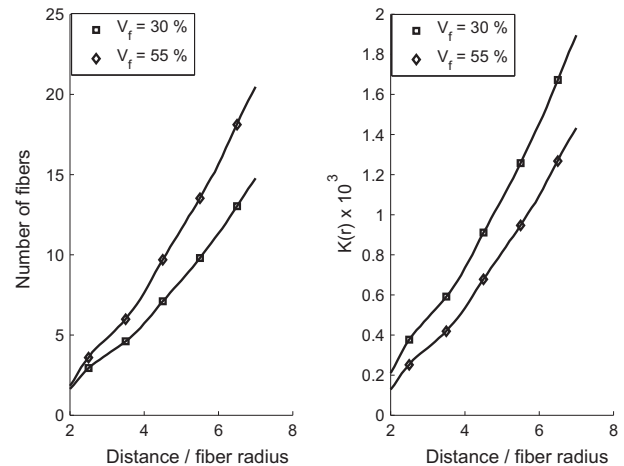

Fig. 6. Average number of fibers as a function of distance from a given fiber: (a) total number of fibers and (b) second-order intensity function.

by the overall fiber density. It is proportional to the integral over the radius of the RDF, and the two functions provide the same information.

Fig. 6 shows the average number of neighbor fibers as a function of distance for samples with two different values of V_f, as well as the corresponding second-order intensity function.

4. Experiments

4.1. Silicone rubber

The modulus and elongation properties in Table 1 were verified experimentally through uniaxial testing. Two different set of values were found, see Fig. 7. For specimens cured in the autoclave, failure typically occurred at 120–140% elongation, with a value of the Cauchy stress of approximately 1.25 MPa. For specimens cured in the oven the values were 100–120% and 1.7–2 MPa, respectively. It is believed that the reason for the difference is the presence of epoxy residue in the autoclave, where traditional composites are often cured.

Fig. 8 shows the stress–stretch and stress–time relationship obtained from tests combining cyclic and relaxation loading. These results show negligible hysteresis or viscoelastic effects, which
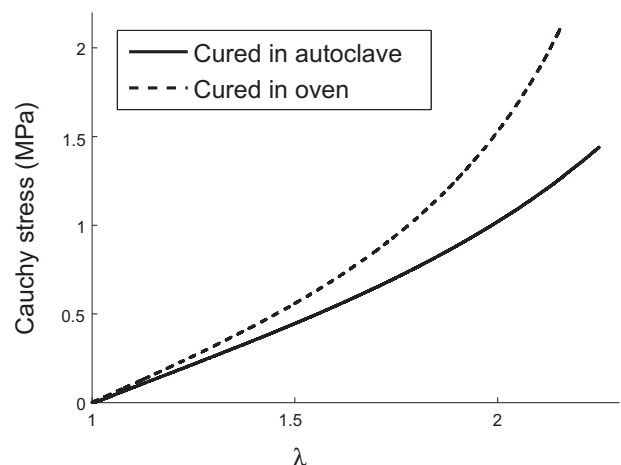

Fig. 5. Micrograph obtained by stacking six images in Photoshop, V_f = 30%.

Fig. 7. Uniaxial stress–stretch relationship of CF19-2615 silicone. The two specimens are taken from the same batch of silicone, the only difference being the curing.
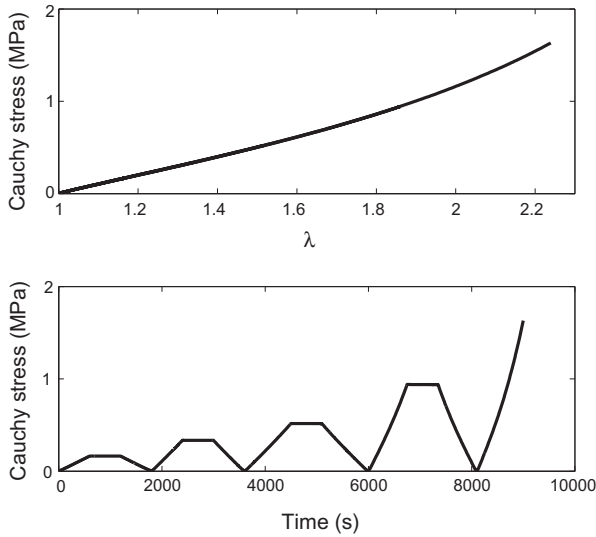
Fig. 8. Uniaxial stress–stretch and stress–time relationship for silicone, obtained from a test involving cyclic loading with holding periods; the silicone had been cured in an oven.

agrees with published test results for silicone rubber (Meunier et al., 2008; Machado et al., 2010). Other types of rubber exhibit strain softening even when they are unreinforced.

4.2. Folding tests

The specimens were put in a fixture that imposes a 90° kink angle and a radius of curvature of approximately 2 mm. Fig. 9 shows the tension and compression side of a specimen with V_f = 30%. Microbuckling can be observed; buckles appear both on the compression and tension sides, but the buckle amplitude is larger on the compression side. This observation agrees with the simulation results shown in Section 6. The experiment was repeated on a specimen with V_f = 55% and similar images were obtained in this case. The existence of buckled fibers on the tension side is typical of very thin composites and does not happen in the case of thicker specimens (Francis, 2008).
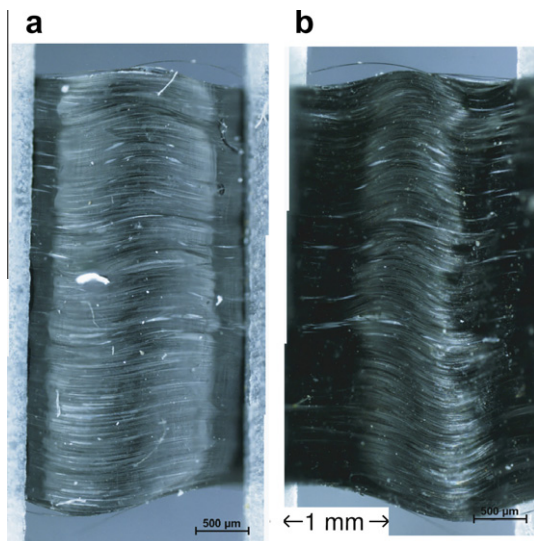

Fig. 9. Specimen with V_f = 30% folded 90° with a 2 mm radius: (a) view of outside of fold region, i.e. tension side of specimen and (b) view of inside of fold region, i.e. compression side of specimen.

4.3. Bending test setup

Standard methods to measure the bending stiffness, such as the four point bending test, are limited to relatively stiff specimens that undergo only small curvatures. In order to measure the non-linear moment–curvature relationship at larger curvatures a different technique is required. In this study the moment–curvature relationship was obtained from the post-buckling behavior of specimens under compressive load.

The specimens, which were 9–15 mm wide, were sandwiched between 0.6 mm thick Aluminium-alloy plates. The plates were glued to the specimens with Instant Krazy Glue, leaving a 4 mm distance between the two pairs of plates, see Fig. 10(a). The sandwiched ends of these specimens are much stiffer than the composite-only strip in the middle and so they can be idealized as rigid.

To reduce the effects of friction and contact the plates were connected with Scotch Magic Tape to rigid blocks attached to the jaws of a materials testing machine (INSTRON 5569 with a 10 N load cell), see Fig. 10(b). Note that the specimen does not touch the blocks at any point during the test: it is connected solely to the tape. The bending stiffness of the tape is much lower than that of the specimen and therefore this connection can be treated as a zero-moment hinge. The specimens were weighed before the test; their total weight, W, including the aluminum plates was approximately 1 g.

A schematic analysis of the test is shown in Fig. 10(c). The vertical displacement $\delta = 2L + b − 2h$ is controlled and the corresponding vertical load measured by the load cell is $F − \frac{W}{2}$, where F is the
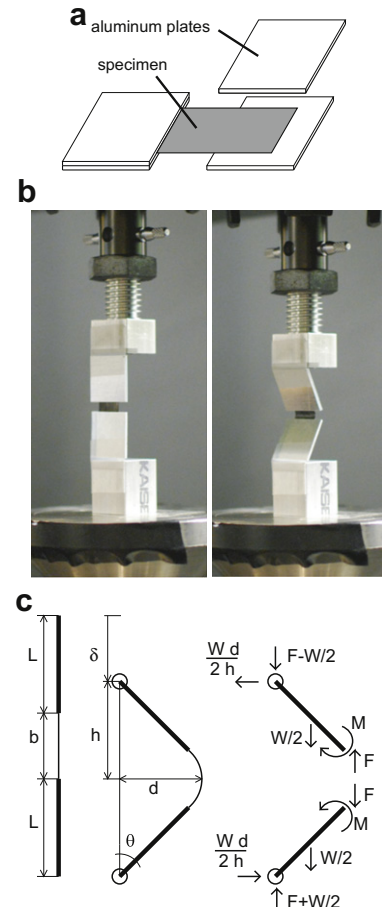

Fig. 10. Test for high curvature bending: (a) preparation of specimen, (b) test setup, showing bending of specimen due to compressive displacement and (c) analysis of geometry and force equilibrium in the test.

vertical force at the center of the specimen. Assuming a uniform curvature, κ, in the specimen the main geometric parameters can be expressed as:

$$\kappa = \frac{2\theta}{b} \tag{5}$$

$$h = L\cos\theta + \frac{b}{2\theta}\sin\theta \tag{6}$$

$$d = L\sin\theta + \frac{b}{2\theta}(1 - \cos\theta) \tag{7}$$

Hence κ can be calculated from the vertical displacement, measured by the testing machine.

The assumption of uniform curvature implies that the moment is uniform within the compliant part of the specimen, and equal to:

$$M = \left(F - \frac{W}{4}\right)d \tag{8}$$

This result is valid when the length of the composite-only strip is small compared to the length of the end plates, $b \ll L$; in the present case $b = 4$ mm and $L = 25.4$ mm. This assumption was checked by comparing the results to a more exact solution using non-uniform curvature: no difference could be observed. Photos of the specimens during the tests also showed uniform curvature.

Neglecting the weight W, the maximum normal stress due to the force F, σ_F, and the maximum stress due to the bending moment, σ_M, can be found from standard beam theory

$$\sigma_F = \frac{F}{bt} \tag{9}$$

$$\sigma_M = \frac{Mt}{2I} = \frac{6Fd}{bt^2} \tag{10}$$

where t is the thickness, b the width, and I the second moment of area of the specimen. From these two equations we find that σ_F and σ_M are related by

$$\sigma_M = \sigma_F \frac{6d}{t} \tag{11}$$

and for the geometry of the present test σ_M is 300–500 times larger than σ_F. For this reason, the effect of F can be neglected and the test treated as applying a pure bending moment.

Table 2 shows the typical dimensions of the specimens used during the tests.

4.4. Bending test results

The results of two sets of bending tests are shown in Figs. 11 and 12. Each test consisted of three cycles with increasing maximum curvature of 0.22, 0.30 and 0.36 mm^{-1} and each cycle was repeated four times. There are clear signs of strain induced stress softening associated with damage; this behavior is discussed in more detail in López Jiménez and Pellegrino (2011).

In this paper we will focus on the loading part of the first cycle in Figs. 11(a) and 12(a), during which the maximum moment value was attained by each specimen. For both specimens the first monotonic loading moment–curvature relationship is approximately linear for low curvatures. At approximately 0.07 mm^{-1} the stiffness

Table 2
Dimensions of bending test specimens.

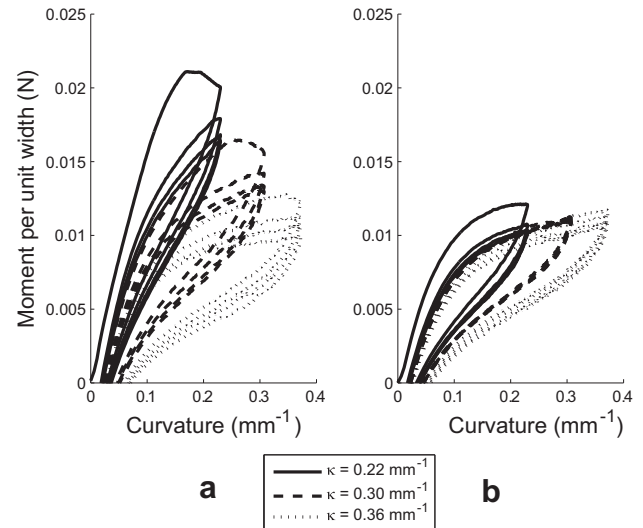|	
Length, b	4 mm
Width	9–15 mm
Thickness – 55% V_f	45 µm
Thickness – 30% V_f	75 µm

Fig. 11. Moment–curvature relationship for a specimen with $V_f = 55\%$, showing strain softening under cycling loading: (a) initial test and (b) test repeated on same specimen after 24 h.
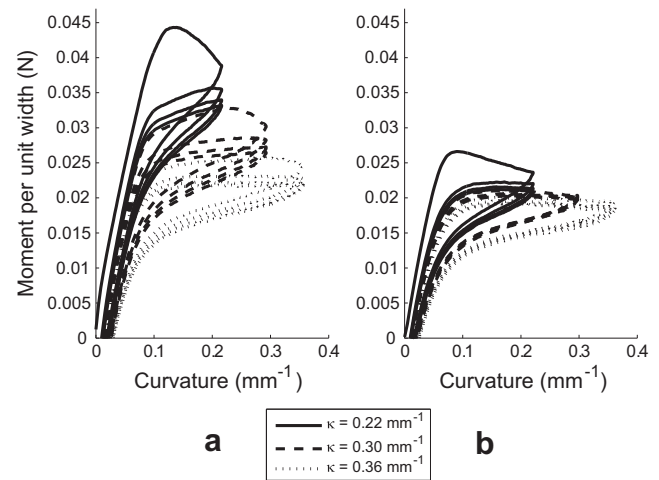

Fig. 12. Moment–curvature relationship for a specimen with $V_f = 30\%$, showing strain softening under cycling loading: (a) initial test and (b) test repeated on same specimen after 24 h.

starts decreasing and for higher curvatures the slope becomes negative.

The tests were performed at three different speeds: 0.25, 0.5 and 1 mm/min of vertical displacement. Note that a uniform vertical displacement rate $\dot{\delta}$ does not translate into a uniform curvature rate $\dot{\kappa}$. Assuming that $b \ll L$, the relationship between the two is given by

$$\dot{\kappa} = \frac{2\dot{\delta}}{Lb\sin\theta} \tag{12}$$

For example, the test geometry show that a uniform vertical displacement rate of 1 mm/min corresponds to curvature rates varying between 0.05 and 0.25 mm^{-1} once the specimen has microbuckled. No significant differences were found and hence rate dependence effects were neglected.

The same two specimens were tested again 24 h after the first test and the results are shown in Figs. 11(b) and 12(b). The damage was not recovered and the stiffness was the same as at the end of the previous test. Both the permanent loss of stiffness and the cycle hysteresis are less pronounced in specimens with lower fiber

volume fraction. This observation agrees with the typical behavior of particle reinforced rubbers discussed in Section 2.

5. Finite element analysis

5.1. Model

A micromechanical finite element model of a bending specimen was set up in the finite element package (Abaqus/Standard, 2007) where both matrix and fibers were modeled with 3D solid elements. Initial attempts to model the fibers with 1D beam elements did not produce useful results, as it is impossible to correctly model the volume fraction of the material and so the stress distribution turns out to be vastly incorrect. The use of 3D elements is required to preserve the geometry of the problem. Bonding between matrix and fibers was assumed to be perfect and therefore both materials share the nodes lying on the contact surfaces.

To reduce the computational cost only a repeating RVE of a tow was modeled: in a study of a tow under bending this RVE must extend through the whole thickness of the tow. Defining the x-axis in the direction of the fibers and the y-axis perpendicular to the midplane of the tow, we considered RVE's resulting from cutting the tow with two planes parallel to the xy plane and at distance W, as seen in Fig. 13. The RVE has length L, width W and height H, as defined in the figure. The arrangement of the fibers within the cross section will be discussed in Section 5.2.

The boundary conditions on the faces of this RVE must ensure periodic behavior in the z direction. Since the meshing of the two faces is identical, periodic boundary conditions were applied directly to corresponding nodes using the EQUATION command in Abaqus. The displacement components in the x and y directions (u and v, respectively) of every node were forced to be equal to those of the corresponding node on the opposite face:

$$u(x, y, 0) = u(x, y, W) \tag{13}$$

$$v(x, y, 0) = v(x, y, W) \tag{14}$$

The difference of displacements in the z direction (w) in each pair of nodes has to be same. This implies that the width of the RVE may change with respect to the undeformed configuration, but it has to be constant through the model:

$$w(x_1, y_1, 0) - w(x_1, y_1, W) = w(x_2, y_2, 0) - w(x_2, y_2, W) \tag{15}$$

The analysis of a RVE is still computationally very expensive if one attempts to model the complete length b of the bending region in a specimen. Instead, it was decided to simulate a piece of material away from the boundaries. In order to achieve this, the only

boundary condition that was applied at the end cross sections is the requirement that the nodes should remain coplanar. The relative position within the plane was left unconstrained, including the displacement in the z direction. The nodes lying in each of these planes were connected to a dummy node, one for each face. Equal and opposite rotations about z, of magnitude θ, were applied to each dummy node. One of the dummy nodes was constrained against translation in all directions, while the other one was left free to translate along the x axis, in order to eliminate all remaining rigid body motions. The faces perpendicular to the y axis were left free.

Müller (1987) showed that the use of RVE's does not ensure finding the correct solution in problems of nonlinear elasticity, such as buckling. Instead, all possible combinations of RVEs should be considered and analyzed. The correct solution is the one corresponding to the lowest energy in the system. This approach has been explored in works studying the non-linear behavior of composite materials, such as buckling of laminates under plane strain (Geymonat et al., 1993).

For the model presented here, Müller's (1987) result implies that the use of a RVE will neglect all possible instabilities with wavelength longer than the size of the cell. This would be a problem if the wavelength of the simulated instability was the same as the length of the model, in which case it is possible that using a larger model would result in a longer wavelength. However, the results presented in Section 6 show that the models used in the present study are able to capture at least half the length of a sinusoidal buckle. Since the minimum wavelength that can be captured by this model is a quarter of a buckle, the length of the model should not affect the computed response. Regarding the number of fibers, models with up to 33 fibers have been used. No difference with respect to smaller models was observed, and this suggests that there are no instabilities dependent on the z coordinate. Such instabilities have not been observed experimentally, either. Therefore it is unlikely that the model neglects an important deformation mechanism due to insufficient width.

The fibers were modeled as a linear elastic material, since the maximum fiber strains observed during the simulations were lower than 1%. The elements used were the solid triangular prisms C3D6 and the material was defined as isotropic since a full orthotropic description of the fibers was not available. Still, a model including five fibers in the RVE was used to perform a comparative study, using typical properties of carbon fibers where no specific data could be found, such as 20 GPa for the orthotropic stiffness. This analysis showed that the main effect of modeling the fibers as orthotropic is a small reduction in the overall bending stiffness.

To obtain some preliminary results the matrix was initially modeled as a linear elastic material but the high strain concentrations, with values of up to 50% even at the initial stages of buckling, made this model numerically unstable even for small applied curvatures. The matrix was then modeled as an incompressible rubber. The elements used were the hybrid square prisms C3D8H. The use of triangular prisms (C3D6 and higher order elements C3D15H) had produced locking due to incompressibility.

Next, two different hyperelastic potentials were used to model the matrix: the Ogden model (Ogden, 1972), implemented in Abaqus as one of the standard material models for rubber, and the model provided by Gent (2005). The second model provided a better fit to the experimental data for the same number of parameters, and hence was adopted for the simulations.

The Gent model was implemented in Abaqus as a user defined material, using the user subroutine UHYPER. The hyperelastic potential is given by:

$$W = -C_1 J_m \ln \left(1 - \frac{J_1}{J_m} \right) + C_2 \ln \left(\frac{J_2 + 3}{3} \right) \tag{16}$$
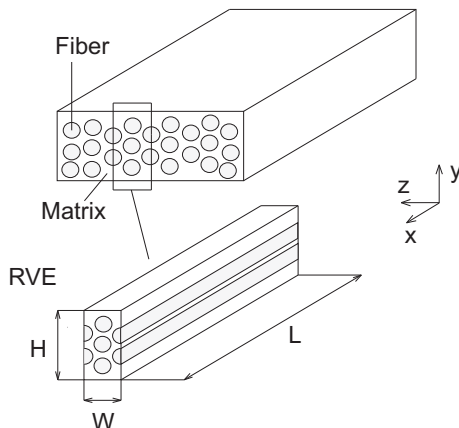

Fig. 13. Representative volume element.

where

$$J_1 = \lambda_1^2 + \lambda_2^2 + \lambda_3^2 - 3 \qquad (17)$$

$$J_2 = \lambda_1^{-2} + \lambda_2^{-2} + \lambda_3^{-2} - 3 \qquad (18)$$

and C_1, C_2 and J_m are parameters to be determined. These parameters were obtained by fitting data to the uniaxial tests presented in Section 4.1. The values obtained were $C_1 = 0.1015$ mJ, $C_2 = 0.1479$ mJ and $J_m = 13.7870$ for the specimens cured in the autoclave and $C_1 = 0.1303$ mJ, $C_2 = 0.1345$ mJ and $J_m = 6.3109$ for those made in the oven.

It must be noted that the strain energy tends to infinity when $J_1 = J_m$. In a uniaxial tension state and for the parameters used in the present study this happens for a value of the elongation well beyond the failure stretch. However, this condition is not implemented in the model and, even if such large values are not reached, the simulation might still need to use them in the middle of an equilibrium iteration. In order to prevent numerical errors the first term in the strain energy equation was substituted by a quadratic function of J_1, and thus the resulting expression is continuous up to the second derivative:

$$W = -C_1 J_m \ln\left(1 - \frac{J_1}{J_m}\right) + C_2 \ln\left(\frac{J_2 + 3}{3}\right) \quad \text{if } J_1 \leqslant 0.9 J_m \qquad (19)$$

$$W = -C_1 J_m \ln(0.1) + \frac{C_1(J_1 - 0.9 J_m)}{0.1} + 0.5 \frac{J_1(J_1 - 0.9 J_m)^2}{0.01 J_m}$$
$$+ C_2 \ln\left(\frac{J_2 + 3}{3}\right) \quad \text{if } J_1 > 0.9 J_m \qquad (20)$$

The most obvious implication of this modification is that the model is stiffer than the real material once the strains in the matrix go beyond the point at which the material should have actually failed. In reality, damage would occur at such large strains, and hence this is a limitation of the present model.

5.2. Arrangement of fibers

Two different approaches to the distribution of fibers in the material were investigated. In the first approach, the fiber axes form an hexagonal grid with a spacing that matches the overall V_f measured from the micrographs. The width of the RVE is such that it contains a column of complete fibers as well as two columns of half fibers (Fig. 14) and the resulting geometry is provided in Table 3.
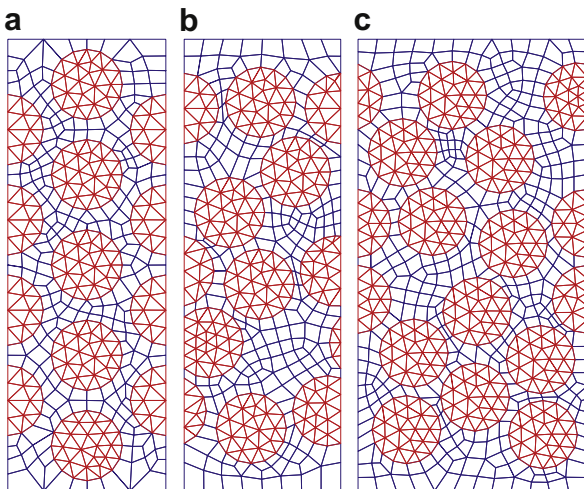

Fig. 14. Examples of RVE's with $V_f = 55\%$: (a) hexagonal pattern; (b) random RVE with the same width as (a); and (c) random RVE with 1.5 times the width of (a).

Table 3
Dimensions of hexagonal RVE's.

Volume fraction	55%	30%
Number of fibers	9	13
Distance between fibers (μm)	8.99	12.17
Height (H) (μm)	40.4	79.1
Width (W) (μm)	15.6	21.1

The hexagonal lattice is a commonly used fiber distribution but micrographs of the material show it is an unrealistic one. Since the fibers are expected to undergo very large deflections the strain energy in the matrix will greatly depend on the spacing between fibers. Random distributions of fibers have been used in works studying the nonlinear deformation of composites under plane strain (Moraleda et al., 2009a,b). Although more realistic, this approach still does not ensure that the geometry of the real material is fully captured. With this objective, a reconstruction based on the approach presented in Rintoul and Torquato (1997) was adopted. The main three steps of the algorithm are presented next.

5.2.1. Initial location of fibers

The number of fibers to be placed in the RVE is calculated according to the volume fraction. The fibers are first allocated randomly within the RVE. For a fiber to be accepted, it cannot be closer than a given value from any of the previously accepted fibers. Otherwise it is discarded, and a new random location is produced. If no suitable location has been found after 1000 attempts, the fiber is accepted anyhow; this limit to the number of attempts is necessary since in cases with $V_f > 50\%$ the process is likely to reach a jamming situation before all the fibers are placed. The minimum distance that needs to be enforced is obviously twice the radius of the fibers. In the present case the value used was 8 μm, that is 1 μm higher than the fiber diameter, to ensure that the matrix between the fibers can be meshed adequately.

If the distance from the center of a fiber to the side in which periodic boundary conditions are applied is less than a fiber radius, then a symmetric fiber must be placed on the other side of the RVE, to satisfy the periodicity of the RVE. In order to avoid poor meshes, fibers whose surface is closer than 1 μm to the edges of the RVE are discarded.

5.2.2. Potential energy

Once all the fibers have been placed, a potential energy E is defined. It will be used to quantify the difference between the current configuration and the goal one, based on several micrographs of the specimen that is being studied. The function used for the reconstruction is the second-order intensity function presented in Section 3.2. The potential is defined as:

$$E = \sum_i \left(K(r_i) - (K_0(r_i))^2 \right) + \sum_j (M\delta_j) \qquad (21)$$

where K_0 is the second-order intensity function observed in the micrographs, the summation in i is made over the intervals used to discretize r, M is a large positive number and δ_i is equal to one if the jth fiber violates one of the rules explained before (such as intersecting with another fiber) and zero otherwise.

5.2.3. Evolution process

A fiber is picked randomly and a random displacement is applied. The potential E' is calculated for this new configuration. If it is lower than the previous value, the displacement is accepted. If it is higher, the displacement is accepted with probability $e^{\frac{E-E'}{A}}$, where A is a parameter that controls how fast the system should evolve (a value of 0.05 has been used in this work). This means that
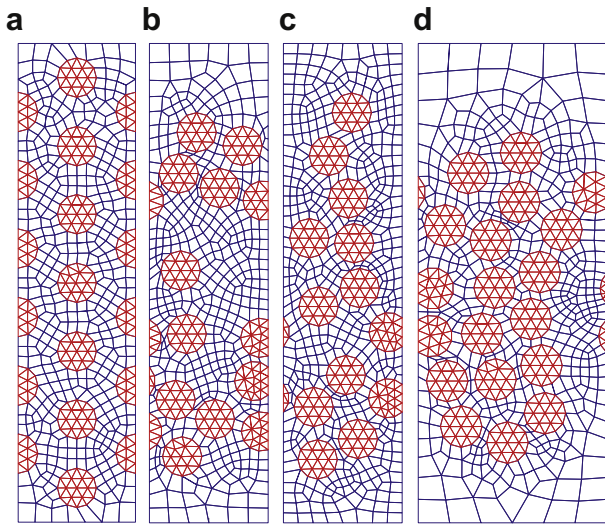
Fig. 15. Examples of RVEs with $V_f = 30\%$: (a) hexagonal pattern, (b) unrealistic random RVE with same width as (c); (b) realistic random RVE with same width as (a); and (d) realistic random RVE with 1.5 times width of (a).

the algorithm would accept some of the displacements in which the energy increases slightly, but almost none implying a large increment.

This last step is repeated until the system converges to a stable value of E. Fig. 14 shows the hexagonal RVE corresponding to $V_f = 55\%$ as well as two examples of random arrangements. The first random cell has the same width as the cell obtained with the hexagonal pattern, while the second one is 50% wider.

In the case $V_f = 55\%$ no dependence on the size of the RVE was observed. By contrast, the width of the specimens was found to be important in the case of lower volume fractions. The reconstruction process tends to group the fibers in clusters, leaving large regions of pure silicone. For example, the reconstruction process might produce a RVE such as that in Fig. 15(b) and, because of the periodic nature of our model, there will be a band without any fibers extending through the whole model. It is possible to produce RVE's with the same size that do not present such problems, Fig. 15(c), although the process has a better outcome with wider RVE's, see Fig. 15(d). The random RVE's used in this work have up to two and half times the thickness of those based on a hexagonal pattern, which corresponds to roughly 30 fibers.

6. Finite element results

The results presented in this section were produced from models with typically 100,000–120,000 nodes and 120,000–150,000 elements. Analyses carried out with finer meshes provided practically identical results, both in terms of macroscopic (wavelength, moment–curvature relationship) and microscopic (strain localization) features.

6.1. Deformed geometry

Figs. 16 and 17 show different views of the deformed configuration obtained from one of the simulations (hexagonal pattern, $V_f = 55\%$). All of the characteristic features of the folding of a fiber composite with a hyperelastic matrix can be seen in these results: in-plane buckling of the fibers, large fiber deflections, larger buckle amplitude on the compression side and uniform curvature. These features are common to all cases, regardless of fiber arrangement and fiber volume fraction. The buckle wavelength ranges from
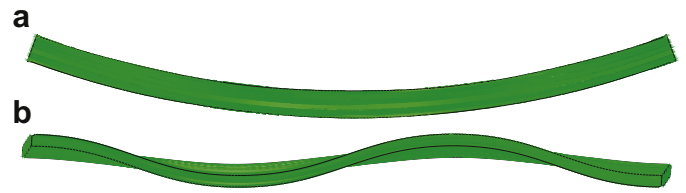

Fig. 16. Views of deformed configurations of RVE with hexagonal fiber arrangement, $V_f = 55\%$ and $L = 1$ mm subject to $\kappa = 0.7$ mm^{-1}: (a) side view and (b) top view.

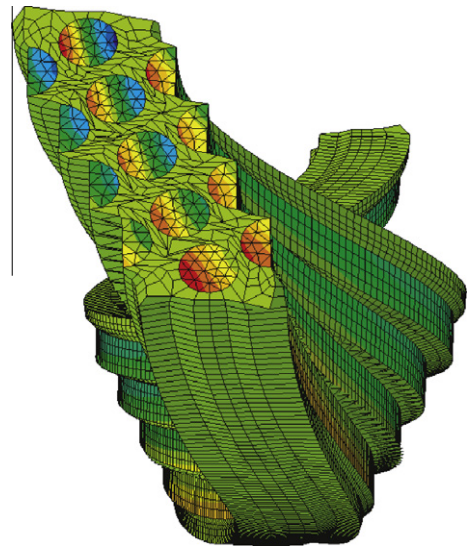**Fig. 17.** Perspective view of RVE showing longitudinal stress field. $V_f = 55\%$, hexagonal fiber arrangement, 1 mm length, $\kappa = 0.7$ mm^{-1}.

0.33 mm to 0.5 mm in the case shown ($V_f = 55\%$) and 0.5 mm to 1 mm in the case $V_f = 30\%$.

It should be noted that the wavelength computed from these simulations is affected by the chosen length L of the RVE, which is 1 mm in all the cases considered. Changing L by a small amount would probably result in the same number of waves and therefore a different wavelength. This effect could be minimized by analyzing a much longer RVE, but this could not be done due to the already high computational cost of the present analysis.

The wavelengths predicted by the simulations are shorter than those observed experimentally for $V_f = 55\%$, although the predictions are much closer for $V_f = 30\%$, see Table 4. Analytical results in Francis (2008), López Jiménez and Pellegrino (2009) show that as the wavelength increases the strain energy of the matrix also increases, while the strain energy of the fibers decreases. The present results are therefore an indication that the finite length of the present model has not allowed the fibers to form buckles of unconstrained length.

6.2. Strains

The evolution of the largest principal strains with the applied curvature can be studied with these models, see Figs. 18 and 19. In the case $V_f = 55\%$ randomness in the fiber distribution does not lead to significant changes in the maximum strains, since the fibers are already densely packed even in the hexagonal arrangement. In the case $V_f = 30\%$ the maximum strains are higher in the case of random fiber arrangement.

Since the buckled fibers are mainly subjected to bending, the maximum and minimum principal strains give a very good indication of the possibility of failure in the material. The failure

Table 4
Comparison of wavelengths from simulations and experiments.

Volume fraction	55%	30%
Simulations	0.33–0.5 mm	0.5–1 mm
Experiments	0.55–0.70 mm	0.6–0.65 mm
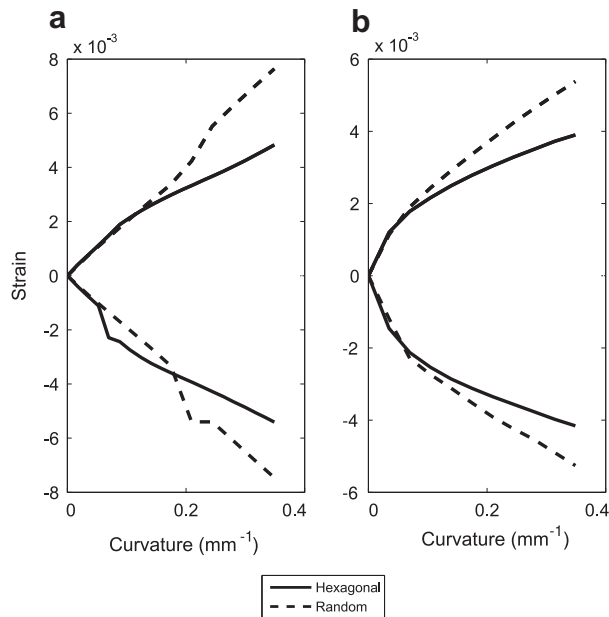
Fig. 18. Maximum and minimum principal strains in the fibers: (a) V_f = 55% and (b) V_f = 30%.

Fig. 19. Maximum and minimum principal strains in the matrix: (a) V_f = 55% and (b) V_f = 30%.

Fig. 20. γ_{yz} strain field for V_f = 55%: (a) hexagonal pattern and (b) random pattern.

elongation of the fibers in Table 1 is 1.8% and the predictions in Fig. 18 are well below this value.

The strain state in the matrix is rather more complex and, since there are no established failure criteria for silicone rubber under multi-axial loading conditions, it is hard to tell what combination of strains or stresses in the matrix would cause failure. Damage processes such as cavitation, debonding between silicone and carbon fibers (which will also depend on the type and amount of sizing used to coat the fibers), breaking and disentanglement of polymer chains, etc. will play a role. Since the largest strains in the matrix provided by the simulations, in excess of 200%, are so much greater than the failure strain obtained from the uniaxial tensile tests in Section 4.1, damage would be expected to occur before reaching such high strains. Hence it can be concluded that our matrix model will tend to become unrealistically stiffer.

The fact that the maximum principal strains in the matrix are similar for hexagonal and random arrangements of the fibers does not mean that the strain states are in fact similar. Fig. 20 shows contour plots of γ_{yz} for two models with V_f = 55%. Both sections shown in this figure correspond to the point of maximum deflection of the buckle, for κ = 0.35 mm^{-1}. In the case of the hexagonal pattern all fibers buckle together, the only difference being in the amplitude, and this produces a regular strain pattern in the matrix. The randomly arranged fibers create a less regular strain distribution, with high positive and negative strains within the same section. In the latter case the amplitude of the buckle is practically the same through the whole thickness and this produces higher strains in both matrix and fibers.

In the case of lower fiber volume fractions the results are similar for the random and regular fiber arrangements, see Fig. 21. In particular, the variation of the fiber buckle amplitude through
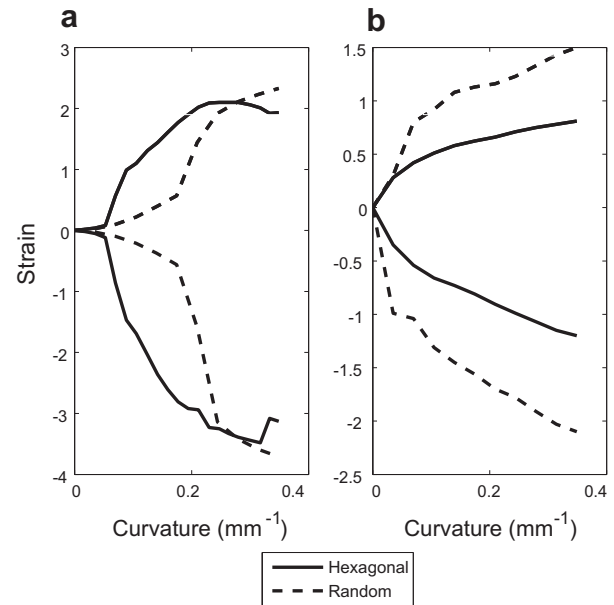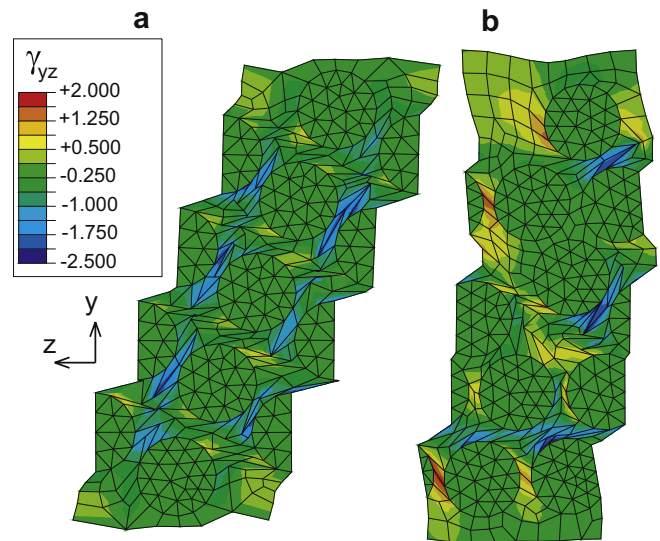
the thickness of the RVE is similar for both arrangements, unlike the previous case.

Simulations based on RVE's with a larger number of fibers give similar results, the main difference being the presence of larger areas of pure silicone, in which the material can shear very easily, see Fig. 22. The use of wider RVE's tends to impose a more homogeneous variation of the buckled amplitude through the thickness.

6.3. Moment vs. curvature

The higher strains observed in the cases with random fiber arrangement correspond to a greater stiffness overall, as can be seen by plotting the moment–curvature relationship. In all plots the curvature is assumed to be uniform along the length of the model and it is therefore calculated by dividing by L the relative rotation applied at the ends. Fig. 23 shows the moment–curvature
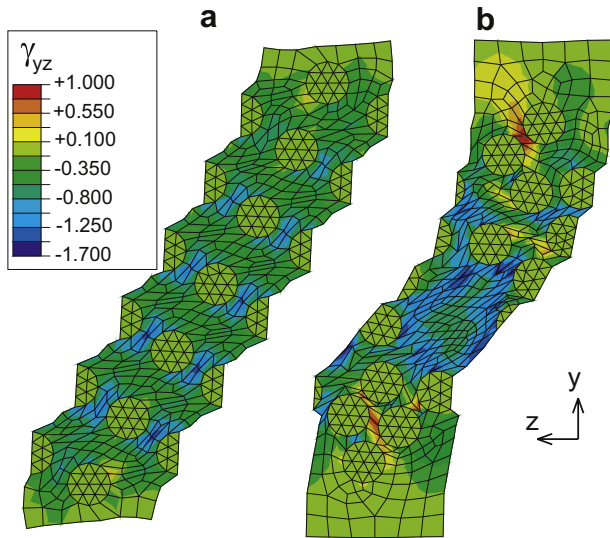
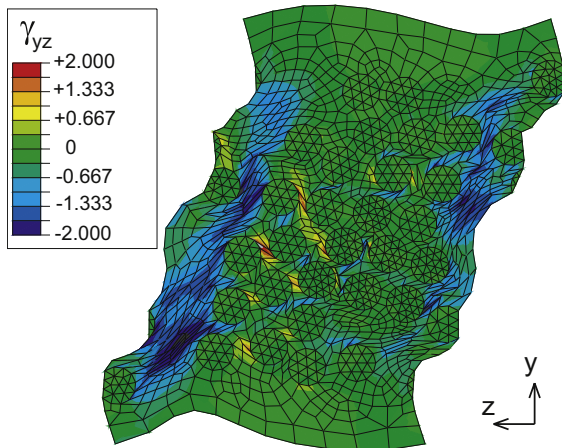**Fig. 21.** γ_{yz} strain field for V_f = 30%: (a) hexagonal pattern and (b) random pattern.

Fig. 22. γ_{yz} strain field for V_f = 30%; the width is 2.5 times that of the RVE with hexagonal fiber arrangement.

Fig. 23. Moment vs. curvature for simulations with V_f = 55%. The plot shows the results from the simulation with hexagonal fiber arrangement, four simulations with random RVE's, and a linear analysis for reference.

Fig. 24. Moment vs. curvature for simulations with V_f = 30%. The plot shows the results from the simulation with hexagonal fiber arrangement, three simulations with random RVE's, and a linear analysis for reference.

Fig. 25. Comparison of moment vs. curvature in simulations and experiments for V_f = 55%. The plot shows the results from the simulation with hexagonal fiber arrangement, the range spanned by the simulations with random RVE, and five experiments; a linear analysis has been added as a reference.

relationship of the simulations with V_f = 55%. The cases with random fiber arrangement show some variation among each other, but they are clearly stiffer than the case with hexagonal pattern. An analysis with linear geometry for the hexagonal pattern is also plotted for comparison: it coincides with the initial response of all cases. Once the fibers have buckled, the stiffness of the regular pattern drops to only about 20% of the initial stiffness, whereas in the case of randomly arranged fibers the stiffness drops to 60–75%.

In the cases with V_f = 30% the responses of the models with regular and random fiber arrangements are much closers and are both much softer than the linear prediction, see Fig. 24. The sudden drop in stiffness is related to the sudden start of microbuckling, which is associated with a drop to a lower state of energy. This produces a discontinuity in the first derivative of the strain energy. This is not likely to occur in the real material, due to the presence of imperfections that will produce a smooth transition to the buckled state. This effect can be reduced by introducing waviness in the fibers, but it is hard to make it disappear completely.

The results of the finite element analysis and the experiments are compared in Figs. 25 and 26, where the area enveloped by the simulations with several different initial geometries of random fibers has been shaded in grey.
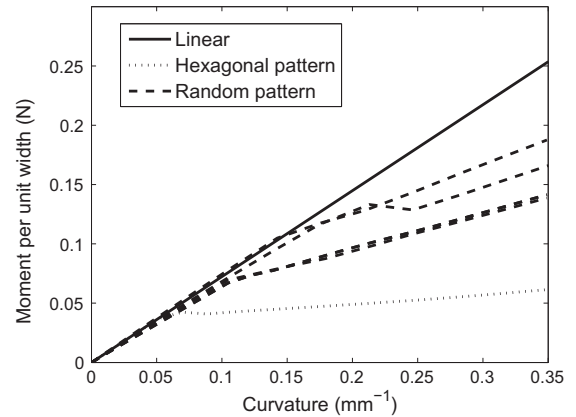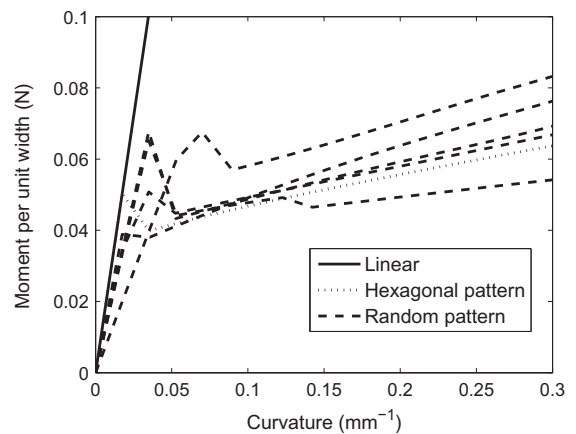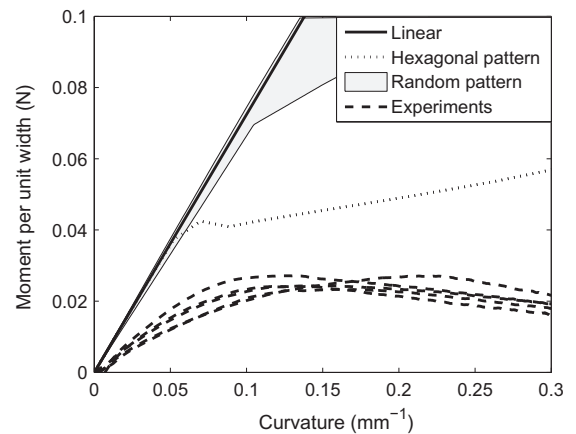
In the first case, V_f = 55%, the prediction is much stiffer than the actually measured behavior. It is believed that there are two main reasons. The first one is the extreme strain concentrations in the
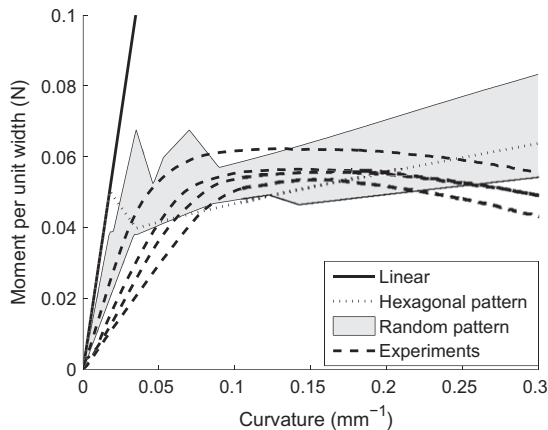
Fig. 26. Comparison of moment vs. curvature in simulations and experiments for $V_f = 30\%$. The plot shows the results from the simulation with hexagonal fiber arrangement, the range spanned by the simulations with random RVE, and four experiments; a linear analysis has been added as a reference.

silicone, as shown earlier in the paper, which would case localized failures; these effects are neglected in the material model. The second reason is the very small thickness of the specimen which, combined with its anisotropy, lead to a high sensitivity to non-uniformity in the thickness of the specimens. These effects result in global deformation modes that cannot be captured by the periodicity assumed in our model.

In the second case, $V_f = 30\%$, the initial stiffness observed in the test lies within the region predicted by the simulations but, once microbuckling takes place, high strains in the matrix would result in localized damage which is, again, not captured by the present model. Overall, the prediction is stiffer than the experimental results although much closer than for $V_f = 55\%$.

7. Discussion and conclusions

A composite material consisting of unidirectional carbon fibers embedded in a silicone matrix was fabricated and its bending properties were studied experimentally. It was found that this material can be folded to very high curvatures without any fiber damage and its moment vs. curvature relationship is highly nonlinear. This behavior is due to the capability of the fibers to micro-buckle within the soft matrix, which provides a stress relief mechanism. Significant strain softening was observed when cyclic loading was applied, which indicates that, although the fibers appear undamaged, actually some damage is introduced.

A finite element model was created in order to study the micro-mechanical behavior of thin sheets of this material when it is folded. The model is based on two main simplifying assumptions. The first one is the use of a small representative volume element to model a much larger piece of material, using periodic boundary conditions. The fiber distribution has been modeled using either a regular hexagonal lattice or a random arrangement based on distributions observed in actual micrographs of the material. The second assumption concerns the behavior of the constituent materials and their interfaces. The fibers were modeled as linear elastic and the matrix as purely hyperelastic; no source of damage or failure was considered and perfect bonding between fibers and matrix was assumed.

The model captures the main features that are observed in the folding experiment, including fiber microbuckling and the overall nonlinear behavior. When comparing the wavelengths and the moment–curvature relationships between simulations and experiments, the cases with $V_f = 30\%$ show good agreement, while in

the case of $V_f = 55\%$ the finite element model predicts a shorter wavelength than that observed in experiments. The model also provides a better prediction of the moment vs. curvature relationship for the material with lower volume fraction, although in both cases it is not able to capture the softening observed in the experiments once microbuckling takes place.

This disagreement appears to be linked to a key assumption adopted in the material model, namely the lack of any damage or dissipation anywhere. The geometry of the fiber composite, coupled with the much higher compliance of the matrix with respect to the fibers, leads to high strain concentrations in the matrix between close fibers. The strains predicted by the present model are much greater than the failure strains measured in uniaxial tests of the matrix, so it is reasonable to assume that the matrix would become damaged before reaching such large strains. This explanation also agrees with the strain softening observed in cyclic tests, which indicates the presence of permanent damage in the material. Observations of the surface of specimens that had been folded to very high curvatures did not show any broken fibers, which suggests that the damage takes place in the matrix or at the interface with the fibers.

In conclusion, the present work has shown that very good results can be achieved with a hyperelastic matrix model for the case of low fiber volume fraction, although the results are less accurate for composites with a high fiber volume fraction. In order to produce a more accurate model for the latter case, it would be necessary to incorporate a damage mechanism able to reduce the strain in the matrix to more realistic values. These issues are beyond the scope of the present study of folding mechanics but a forthcoming paper López Jiménez and Pellegrino (2011) proposes a different test that focuses specifically on the study of nonlinearities due to material damage.

References

Abaqus/Standard, 2007. Software, Ver. 6.7, Simulia, Providence, RI.
Adobe Photoshop CS4, 2008. Software, Adobe, San Jose, CA.
Agoras, M., Lopez-Pamies, O., Ponte Castañeda, P., 2009. A general hyperelastic model for incompressible fiber-reinforced elastomers. Journal of the Mechanics and Physics of Solids, 268286.
Auternaud, J., Bartevian, J., Bertheux, P., Blanc, E., de Mollerat du Jeu, T., Foucras, J., Louis, M., Marello, G., Poveda, P., Roux, C. 1993. Self-Motorized Antifriction Joint and an Articulated Assembly, such as a Satellite Solar Panel, Equipped with such Joints. US Patent 5,086,541.
Barrett, R., Francis, W., Abrahamson, E., Lake, M.S., Scherbarth, M., 2006. Qualification of elastic memory composite hinges for spaceflight applications. In: 47th AIAA/ASME/ASCE/AHS/ASC Structures, Structural Dynamics, and Materials Conference, Newport, Rhode Island, AIAA 2006-2039.
Campbell, D., Lake, M., Mallick, K., 2004. A study of the bending mechanics of elastic memory composites. In: 45th AIAA/ASME/ASCE/AHS/ASC Structures, Structural Dynamics, and Materials Conference, Palm Springs, CA.
Campbell, D., Lake, M., Scherbarth, M., Nelson, E., Six, R.W., 2005. Elastic memory composite material: An enabling technology for future furlable space structures. In: 46th AIAA/ASME/ASCE/AHS/ASC Structures, Structural Dynamics, and Materials Conference, Austin, TX.
Datashvili, L., Nathrath, N., Lang, M., Baier, H., Fasold, D., Pellegrino, S., Soykasap, O., Kueh, A., Tan, L.T., Mangenot, C., Santiago-Prowald, S., 2005. New concepts and reflecting materials for space borne large deployable reflector antennas. In: 28th ESA Antenna Workshop on Space Antenna Systems and Technologies, 31 May–3 June 2005, ESTEC, Noordwijk, The Netherlands.
Datashvili, L., Baier, H., Wehrle, E., Kuhn, T., Hoffmann, J., 2010. Large shell-membrane space reflectors. In: 51st AIAA/ASME/ASCE/AHS/ASC Structures, Structural Dynamics, and Materials Conference, Orlando, Florida.

Dorfmann, A., Ogden, R.W., 2004. A constitutive model for the Mullins effect with permanent set in particle-reinforced rubber. International Journal of Solids and Structures, 1855–1878.

Drapier, S., Garding, C., Grandidier, J.C., Potier-Ferry, M., 1996. Structure effect and microbuckling. Composites Science and Technology 56, 861–867.

Drapier, S., Grandidier, J.C., Potier-Ferry, M., 1999. Towards a numerical model of the compressive strength for long fibre composites. European Journal of Mechanics A/Solids 18, 69–92.

Drapier, S., Grandidier, J.C., Potier-Ferry, M., 2001. A structural approach of plastic microbuckling in long fibre composites: comparison with theoretical and experimental results. International Journal of Solids and Structures 38, 3877–3904.

Fleck, N.A., 1997. Compressive failure of fiber composites. Advances in Applied Mechanics 33, 43–117.

Francis, W.H., 2008. Mechanics of Post-Microbuckled Compliant-Matrix Composites. Master's Thesis. Colorado State University.

Francis, W.H., Lake, M., Steven Mayes, J., 2006. A review of classical fiber microbuckling analytical solutions for use with elastic memory composites. In: 47th AIAA/ASME/ASCE/AHS/ASC Structures, Structural Dynamics, and Materials Conference, Newport, RI.

Fung, Y., 1972. Biomechanics***,, .. Mechanical Properties of Living Tissues, second ed. Springer, New York.

Gent, A.N., 2005. Elastic instabilities in rubber. International Journal of Non-Linear Mechanics 40, 165–175.

Geymonat, G., Mller, S., Triantafyllidis, N., 1993. Homogenization of nonlinearly elastic materials, microscopic bifurcation and macroscopic loss of rank-one convexity. Archive for Rational Mechanics and Analysis 122, 231–290.

Govindjee, S., Simo, J., 1991. A micro-mechanically based continuum damage model for carbon black-filled rubbers incorporating Mullins' effect. Journal of the Mechanics and Physics of Solids 39, 87–112.

Holzapfel, G.A., Gasser, T.C., Ogden, R.W., 2000. A new constitutive framework for arterial wall mechanics and a comparative study of material models. Journal of Elasticity 61, 1–48.

López Jiménez, F., Pellegrino, S., 2009. Folding of thin-walled composite structures with a soft matrix. In: 50th AIAA/ASME/ASCE/AHS/ASC Structures, Structural Dynamics, and Materials Conference, Palm Springs, California.

López Jiménez, F., Pellegrino, S., 2011. Constitutive modeling of fiber composites with a soft hyperelastic matrix. International Journal of Solids and Structures, accepted for publication.

Lopez-Pamies, O., Idiart, M.I., 2010. Fiber-reinforced hyperelastic solids: a realizable homogenization constitutive theory. Journal of Engineering Mathematics.

Lopez-Pamies, O., Ponte Castañeda, P., 2006. On the overall behavior, microstructure evolution, and macroscopic stability in reinforced rubbers at large deformations: I. Application to cylindrical fibers. Journal of the Mechanics and Physics of Solids 54, 831863.

Machado, G., Chagnon, G., Favier, D., 2010. Analysis of the isotropic models of the mullins effect based on filled silicone rubber experimental results. Mechanics of Materials 42, 841–851.

Marissen, R., Brouwer, H.R., 1999. The significance of fibre microbuckling for the flexural strength of a composite. Composites Science and Technology, 327–330.

Mejia-Ariza, J.M., Guidanean, K., Murphey, T.M., Biskner, A., 2010. Mechanical characterization of lgarde elastomeric resin composite materials. In: 51st AIAA/ASME/ASCE/AHS/ASC Structures, Structural Dynamics, and Materials Conference.

Mejia-Ariza, J.M., Pollard, E.L., Murphey, T.W., 2006. Manufacture and experimental analysis of a concentrated strain based deployable truss structure. In: 47th AIAA/ASME/ASCE/AHS/ASC Structures, Structural Dynamics, and Materials Conference, Newport, Rhode Island.

Merodio, J., Ogden, R.W., 2002. Material instabilities in fiber-reinforced nonlinearly elastic solids under plane deformation. Archies of Mechanics 54, 525–552.

Merodio, J., Ogden, R.W., 2003. Instabilities and loss of ellipticity in fiber-reinforced compressible non-linearly elastic solids under plane deformation. International Journal of Solids and Structures 40, 4707–4727.

Meunier, L., Chagnon, G., Favier, D., Orgéas, L., Vacher, P., 2008. Mechanical experimental characterization and numerical modelling of an unfilled silicone rubber. Polymer Testing 27, 765–777.

Moraleda, J., Segurado, J., Llorca, J., 2009a. Effect of interface fracture on the tensile deformation of fiber-reinforced elastomers. International Journal of Solids and Structures 46, 4287–4297.

Moraleda, J., Segurado, J., Llorca, J., 2009b. Finite deformation of incompressible fiber-reinforced elastomers: A computational micromechanics approach. Journal of the Mechanics and Physics of Solids 57, 1596–1613.

Müller, S., 1987. Homogenization of nonconvex integral functionais and cellular elastic materials. Archive for Rational Mechanics and Analysis 99, 189–212.

Murphey, T.W., Meink, T., Mikulas, M.M., 2001. Some micromechanics considerations of the folding of rigidizable composite materials. In: 42nd AIAA/ASME/ASCE/AHS/ASC Structures, Structural Dynamics, and Materials Conference.

NuSil Silicone Technology, March 2007. <http://www.nusil.com/library/products/CF19-2615P.pdf>.

Ogden, R.W., 1972. Large deformation isotropic elasticity – on the correlation of theory and experiment for incompressible rubberlike solids. Proceedings of the Royal Society of London 326, 565–584.

Pandolfi, A., Holzapfel, G.A., 2008. Three-dimensional modeling and computational analysis of the human cornea considering distributed collagen fibril orientations. Journal of Biomechanical Engineering, 130.

Pandolfi, A., Manganiello, F., 2006. A model for the human cornea: constitutive formulation and numerical analysis. Biomechanics and Modeling in Mechanobiology 5, 237–246.

Parnes, R., Chiskis, A., 2002. Buckling of nano-fibre reinforced composites: a re-examination of elastic buckling. Journal of the Mechanics and Physics of Solids 50, 855–879.

Ponte Castañeda, P., 2002. Second-order homogenization estimates for nonlinear composites incorporating field fluctuations: I. Theory. Journal of the Mechanics and Physics of Solids, 737757.

Pyrz, R., 1994a. Correlation of microstructure variability and local stress field in two-phase materials. Materials Science and Engineering 177, 253–259.

Pyrz, R., 1994b. Quantitative description of the microstructure of composites: Part I. Morphology of unidirectional composite systems. Composites Science and Technology 50, 197–208.

Rehnmark, F., Pryor, M., Holmes, B., Schaechter, D., Pedreiro, N., Carrington, C., 2007. Development of a deployable nonmetallic boom for reconfigurable systems of small spacecraft. In: 48th AIAA/ASME/ASCE/AHS/ASC Structures, Structural Dynamics, and Materials Conference, Honolulu, Hawaii.

Rimrott, F.P.J., 1966. Storable tubular extendible members. Engineering Digest September.

Rintoul, M., Torquato, S., 1997. Reconstruction of the structure of dispersions. Journal of Colloid and Interface Science 186, 467–476.

Rosen, B., 1965. Fiber Composite Materials. Metals Park, Ohio.

Schultz, M.R., Francis, W.H., Campbell, D., Lake, M.S., 2007. Analysis techniques for shape-memory composite structures. In: 48th AIAA/ASME/ASCE/AHS/ASC Structures, Structural Dynamics, and Materials Conference, Honolulu, HI.

Spencer, A.J.M., 1972. Constitutive theory of strongly anisotropic solids. In: for Mechanical Sciences, I.C. (Ed.), Continuum Theory of the Nechanics of Fibre-reinforced Composites.

Toho Tenax, retrieved August 2010. <http://www.tohotenax.com/tenax/en/products/st_property.php>.

Watt, A.M., Pellegrino, S., 2002. Tape-spring rolling hinges. In: 36th Aerospace Mechanisms Symposium, NASA Glenn Research Center, May 15–17, 2002.

Yee, J.C.H., Soykasap, O., Pellegrino, S., 2004. Carbon fibre reinforced plastic tape springs. In: 45th AIAA/ASME/ASCE/AHS/ASC Structures, Structural Dynamics and Materials Conference, Palm Springs, CA, 19-22 April 2004, AIAA 2004-1819.

Yee, J.C.H., Pellegrino, S., 2005. Composite tube hinges. Journal of Aerospace Engineering 18, 224–231.